

## Article

# MOF Embedded and Cu Doped CeO<sub>2</sub> Nanostructures as Efficient Catalyst for Adipic Acid Production: Green Catalysis

Shabahat Bibi<sup>1</sup>, Erum Pervaiz<sup>1,\*</sup> , Minghui Yang<sup>2</sup> and Osama Rabi<sup>1</sup>

<sup>1</sup> Heterogeneous Catalysis Lab, Department of Chemical Engineering, School of Chemical & Materials Engineering (SCME), National University of Sciences & Technology (NUST), Sector H-12, Islamabad 44000, Pakistan; sbibi\_che4@scme.nust.edu.pk (S.B.); orabi.che6@scme.nust.edu.pk (O.R.)

<sup>2</sup> Solid State functional Materials Research Lab, Ningbo Institute of Materials Technology and Engineering (NIMTE), Chinese Academy of Sciences (CAS), Ningbo 315201, China; myang@nimte.ac.cn

\* Correspondence: erum.pervaiz@scme.nust.edu.pk; Tel.: +92-51-90855113

**Abstract:** Greatly efficient chemical processes are customarily based upon a catalyst activating the process pathway to achieve higher yields of a product with desired specifications. Catalysts capable of achieving good performance without compromising green credentials are a pre-requisite for the development of a sustainable process. In this study, CeO<sub>2</sub> nanoparticles were tested for their catalytic activity with two different configurations, one as a hybrid of CeO<sub>2</sub> nanoparticles with Zeolitic Imidazole Framework (ZIF-67) and second being doped Cu cations into CeO<sub>2</sub> nanoparticles. Physicochemical and catalytic activity was investigated and compared for both systems. Each hybrid was synthesized by embedding the CeO<sub>2</sub> nanoparticles into the microporous structure of ZIF-67, and Cu doped CeO<sub>2</sub> nanoparticles were prepared by a facile hydrothermal route. As a catalytic test, it was employed for the oxidation of cyclohexene to adipic acid (AA) as an alternative to expensive noble metal-based catalysts. Heterogeneous ZIF-67/CeO<sub>2</sub> found catalytical activity towards the oxidation of cyclohexene with nearly complete conversion of cyclohexene into AA under moderate and co-catalyst free reaction conditions, whereas Cu doped CeO<sub>2</sub> nanoparticles have shown no catalytic activity towards cyclohexene conversion, depicting the advantages of the porous ZIF-67 structure and its synergistic effect with CeO<sub>2</sub> nanoparticles. The large surface area catalyst could be a viable option for the green synthesis of many other chemicals.

**Keywords:** MOFs; ZIF-67; CeO<sub>2</sub>; adipic acid; green catalyst



**Citation:** Bibi, S.; Pervaiz, E.; Yang, M.; Rabi, O. MOF Embedded and Cu Doped CeO<sub>2</sub> Nanostructures as Efficient Catalyst for Adipic Acid Production: Green Catalysis. *Catalysts* **2021**, *11*, 304. <https://doi.org/10.3390/catal11030304>

Received: 7 September 2020

Accepted: 12 January 2021

Published: 26 February 2021

**Publisher's Note:** MDPI stays neutral with regard to jurisdictional claims in published maps and institutional affiliations.



**Copyright:** © 2021 by the authors. Licensee MDPI, Basel, Switzerland. This article is an open access article distributed under the terms and conditions of the Creative Commons Attribution (CC BY) license (<https://creativecommons.org/licenses/by/4.0/>).

## 1. Introduction

Catalysis, which is defined as speeding up of a chemical reaction through a substance that is not consumed itself, is critically important for all areas of modern-day life. Catalysis is eventually involved in the preparation of over 80% of all synthetic products. It is significant not only because it aids the world's economic development, but also because it allows the manufacturing of those materials that sustain the society and human environment. A heterogeneous catalyst is usually preferred in industry as it can be easily separated from the products and permits any side reactions to take place. Recently, CeO<sub>2</sub> has gained huge interest in the field of catalysis due to its high thermal and chemical stability, oxygen vacancies and exceptional functionalities. CeO<sub>2</sub> nanocrystalline particles are interesting because of their diverse area of applications in the fields of catalysis, fuel cells, UV absorbance, electronics, and biomedicine [1–6]. This is because CeO<sub>2</sub> has excellent properties of shuffling between the valence states of 4<sup>+</sup> and 3<sup>+</sup>, generating oxygen vacant defects, and high oxygen storage capability [7–9]. In general, the catalytic activity and reducibility of CeO<sub>2</sub> depends on its surface oxygen content, therefore increasing the concentration of accumulated active oxygen on the surface of CeO<sub>2</sub> would result in its higher catalytic activity. This positioning of oxygen atoms on the surface of CeO<sub>2</sub> is influenced by different components, such as the reaction sites available on the surface of CeO<sub>2</sub> along with its elemental combination, as well

as its oxygen vacancy defects [10–13]. Overall, the morphology-dependent growth of CeO<sub>2</sub> nano frameworks has been reported by many researchers to support their catalytically advanced behavior. Rhombic dodecahedral CeO<sub>2</sub> hollow structures were fabricated by a single-step metal organic framework (MOF)-templated route and a hydrothermal method to demonstrate its improved performance in combustion reactions. This, in fact, increased the specific surface area of CeO<sub>2</sub> and hence resulted in better redox characteristics [14,15]. Additionally, nano CeO<sub>2</sub> with rod-like morphology, predominated by a (110) lattice plane, through a simple hydrothermal approach, has been shown to exhibit superior catalytic performance for CO oxidation, in comparison to CeO<sub>2</sub> nanocubes encased by six lattice planes of (200) [16]. The ratio of the Ce (cerium) precursor and the ionic liquid used for its synthesis is one of the key factors used in controlling the growth of CeO<sub>2</sub> nanoparticles [17]. Nevertheless, morphology-dependent growth of CeO<sub>2</sub> is limited to either the template used or inner structure of the nanocrystal. CeO<sub>2</sub> films of various thicknesses have also been synthesized for the adsorption of hydrocarbons and their hydrophobic nature [18,19]. Here, the thickness played the key role in determining the surface morphology, microstructure, and properties of the films. Thicker films exhibited more adsorption of C-C/C-H on the surface of CeO<sub>2</sub> because of the presence of more oxygen vacancies on thicker films [14]. Embedding metal or metal oxide nanoparticles into metal organic frameworks (MOFs) is a new approach to studying the unique physical and chemical behaviors possessed by metal nanoparticles and their oxides [20,21]. These can be formed by either inserting a pre-synthesized metal nanoparticle into an already prepared MOF or employing that MOF as a template [22,23]. In this context, ZIF-67 has been reported to act as a template capable of thermal decomposition and encasing ceria nanowires, hence shown to have enhanced catalytic ability for heterogenous catalysis [24]. Moreover, Pd, Ru, and Zn cations have also been uniformly embedded into MOFs through facile strategies [25–27]. This further encourages the generation of active metal@MOFs catalysts with excellent stability and catalytic behavior. The idea of embedding CeO<sub>2</sub> nanoparticles into ZIF-67 would be a promising catalyst, as it reduces the agglomeration of CeO<sub>2</sub> nanoparticles when enclosed by the porous structure of ZIF-67, and hence can result in a synergistic impact of metal oxide embodied by a MOF. Keeping that in mind, we have embedded nanoparticles into the mesoporous structure of ZIF-67 through a facile technique, and employed it as a catalyst for the production of adipic acid through oxidation of cyclohexene, as an alternative to expensive noble metal-based catalysts.

Adipic acid (AA) is an important commercial organic compound, used primarily for the production of nylon 6,6. In addition, AA is extensively utilized in fertilizers, lubricants, paper, waxes, and the biomedical and food industries [28–31]. Globally, the production of adipic acid exceeds 3.5 million metric tons with a fast growing requirement of 4% annually [32]. Conventionally, AA is produced by the oxidation of cyclohexanol and cyclohexanone (so-called ketone-alcohol oil) with nitric acid (HNO<sub>3</sub>), in majority industrial processes, in the presence of copper (II) or vanadium as catalysts [33]. Although this process is economically viable, the reduction of HNO<sub>3</sub> produces NO<sub>x</sub> as by-products. Amongst them, NO and NO<sub>2</sub> are recycled but N<sub>2</sub>O<sub>5</sub> and N<sub>2</sub>O are released in the atmosphere, thus adding to global warming and ozone depletion [33,34]. Taking that into account, researchers have devoted their efforts to developing effective and environmentally friendly methods for the industrial production of adipic acid that do not employ HNO<sub>3</sub> as oxidant. For that purpose, utilizing H<sub>2</sub>O<sub>2</sub> and molecular oxygen as oxidants has been widely employed [35–37]. H<sub>2</sub>O<sub>2</sub> decomposes to water as a by-product and thus its application in producing adipic acid relates to establishing sustainable processes. However, its usage in concentrations more than 60%, is intricate for safety reasons [38,39]. On the other hand, scientists have also worked on the usage of renewable feedstock for the production of AA, such as glucose, which is biologically converted into AA by the use of microorganisms [40]. Even though these processes are eco-friendly, their prolonged reaction times and comparatively lower yields of adipic acid make them commercially not viable. Noble metal-based catalysts have been reported to effectively catalyze the cyclohexene oxidation

to adipic acids such as Pd, Rh and Au [41–43]. The very first process that utilized  $\text{H}_2\text{O}_2$  as an oxidant for the production of adipic acid was reported by Sato et al. [38]. Cheng et al. presented their work on the modification of an SBA-15 mesoporous catalyst with tungsten oxide to catalyze the production of adipic acid through oxidation of cyclohexene [44]. In that process, the yield of the product achieved was 30% at 85 °C after 13 h. Saedi et al. studied the oxidation of cyclohexene by using MIL-101 metal organic framework as a heterogenous catalyst [45]. This produced high to excellent yields of adipic acid, while MIL-101 was also proved to be a reusable catalyst. The titanium- and cerium-containing mesoporous silicate materials Ti-MMM-2 and Ce-SBA-15 have also been employed as catalysts for cyclohexene oxidation to adipic acid with aqueous  $\text{H}_2\text{O}_2$  under solvent-free conditions [46]. In comparison to conventional MOFs, reports on catalytic studies of ZIF-67 for organic transformations are limited in the literature. To our knowledge, this is the first time that ZIF-67/ $\text{CeO}_2$  has been employed for the oxidation of cyclohexene into adipic acid, using  $\text{H}_2\text{O}_2$  as an oxidant. Doping  $\text{CeO}_2$ , with metal cations is another approach to developing hybrid nanostructures with modified surface elemental combinations. It results in the enhanced chemical behavior of ceria nano frameworks because of the increased oxygen deformities on its surface [47]. For instance,  $\text{CeO}_2$  doped with a minor concentration of  $\text{Y}^{3+}$  has been reported to result in an extremely distributive pattern of dopant cations that bonded with the surface oxygen vacancies uniformly, and thus increased the reducibility and catalytic capability of the material [48]. Similarly, many reports have been presented on  $\text{CeO}_2$  doped with copper or  $\text{CuO-CeO}_2$  nanocomplexes. The collaboration of  $\text{CeO}_2$  with  $\text{CuO}$  is a solid role of  $\text{CeO}_2$  crystalline size. By incorporating a transition metal, a narrow crystalline size of  $\text{CeO}_2$  favors the generation of exceedingly reducible oxygen species [49,50].

In our study, a performance comparison of MOF embedded  $\text{CeO}_2$  nanoparticles with its metal doped structure are presented, with an adequate understanding of the enhanced catalytic and reducible properties of  $\text{CeO}_2$ . For the MOF, we have chosen ZIF-67, due to its better thermal and chemical stability and dodecahedral morphology. On the other hand, Cu doped  $\text{CeO}_2$  nanospheres have been prepared by a simplistic hydrothermal route. For analyzing its catalytic capability, ZIF-67/ $\text{CeO}_2$  is used as a catalyst to produce adipic acid through the oxidation of cyclohexene.

## 2. Results and Discussion

The indexed XRD (X-ray Diffraction) pattern of  $\text{CeO}_2$  nanoparticles prepared through a hydrothermal method, with the  $\text{Ce}^{3+}/\text{OH}^-$  ratio of 1:1, is shown in Figure 1a.

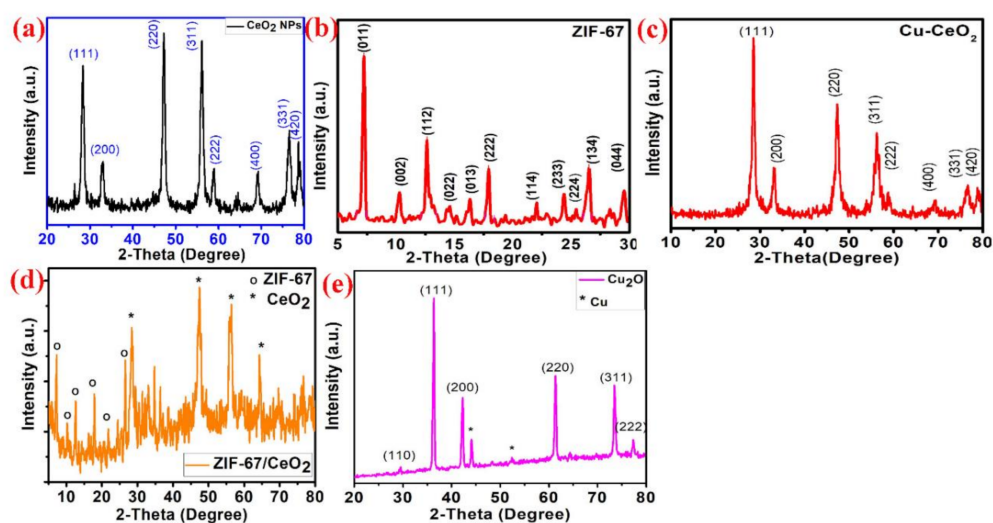


**Figure 1.** The indexed XRD patterns of (a) pure  $\text{CeO}_2$  nanoparticles (b) pure ZIF-67 (c) 10% Cu doped  $\text{CeO}_2$  (d) nanohybrid of ZIF-67/ $\text{CeO}_2$  (e) 90% Cu doped  $\text{CeO}_2$  ( $\text{Cu}_2\text{O}$ ).

The obtained diffraction peaks can be ascribed to the face centered cubic (FCC) fluorite structure of  $\text{CeO}_2$  ( $a = 0.5411 \text{ nm}$ ) [51]. The higher intensity peaks were obtained at  $28.53^\circ$ ,  $47.5^\circ$  and  $56.26^\circ$ , corresponding to the crystal planes of (111), (220) and (311), respectively. It is previously reported that  $\text{Ce}^{3+}/\text{OH}^-$  ratio has large effect on size and crystallinity of ceria nanoparticles [51]. Herein, we have used 1:1 ratio of  $\text{Ce}^{3+}/\text{OH}^-$  to obtain well-dispersed crystalline ceria nanoparticles. The crystallite size of  $\text{CeO}_2$  calculated from the Scherrer formula is 8 nm. Figure 1b shows the XRD pattern of as-prepared ZIF-67 polyhedrons, which counterparts well with the already reported data, illustrating that the as-prepared ZIF-67 polyhedrons are crystalline with pure phase [52]. The sharp and narrow peaks in the XRD pattern demonstrate the high crystallinity of ZIF-67 polyhedral structures [52]. Figure 1c displays the XRD pattern of Cu doped  $\text{CeO}_2$  with 10% molar ratio of  $\text{Cu}^{2+}$ . All the diffraction peaks shown in the pattern correspond to the FCC fluorite structure of ceria, with no sign of  $\text{CuO}$ ,  $\text{Cu}_2\text{O}$ , or  $\text{CeOHCO}_3$ , which demonstrates the uniformity of the doping in the parent lattice of  $\text{CeO}_2$  [53]. The narrow and strong peaks confirm the formation of a well crystalline Cu doped  $\text{CeO}_2$  with an average crystallite size of 40 nm. Figure 1d presents the XRD pattern of ZIF-67/ $\text{CeO}_2$  hybrid nanostructures. It can be seen from the XRD pattern that diffraction peaks for ZIF-67 and  $\text{CeO}_2$  are both present at specific 2-theta positions. The diffraction peaks of  $\text{CeO}_2$  that is encapsulated/dispersed into polyhedral ZIF-67 are equally visible because of its well crystalline nature. The peaks from 5 to  $28^\circ$  are ascribed to the presence of ZIF-67, while further peaks from  $30$  to  $80^\circ$  confirm the presence of  $\text{CeO}_2$  nanoparticles in the prepared hybrid. Figure 1e represents the XRD pattern of 90 mol%  $\text{Cu}^{2+}$  in  $\text{CeO}_2$  prepared by the same route. It can be seen that the XRD pattern matches well with the pure  $\text{Cu}_2\text{O}$  crystalline phase with no impurity peak for Ce or  $\text{CeO}_2$ . This shows that increasing the amount of Cu cations during doping has resulted the deformation of the crystalline phase and instead of the  $\text{CeO}_2$  phase, a pure  $\text{Cu}_2\text{O}$  phase is observed. This is why dopant concentration was limited till 10 mol%  $\text{Cu}^{2+}$ . To investigate the morphology of the prepared samples, SEM (scanning electron microscopy) images were obtained, which are shown in Figure 2.

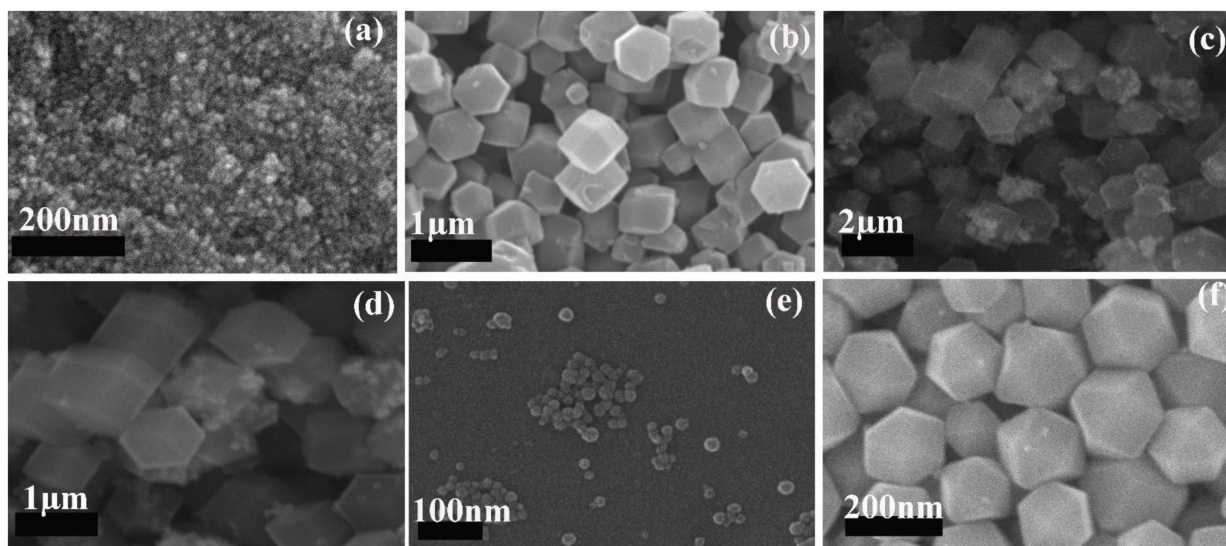


**Figure 2.** SEM images of (a) pure  $\text{CeO}_2$  (b) pure ZIF-67 (c,d) low- and high-resolution SEM of ZIF-67/ $\text{CeO}_2$  (e) 10% Cu doped  $\text{CeO}_2$  (f) 90% Cu doped  $\text{CeO}_2$ .

The spherical morphology of  $\text{CeO}_2$  nanoparticles is shown in Figure 2a, where dispersed spheres of small size can be perceived. The average diameter is speculated to be in the range of 24–33 nm (the corresponding SEM image, displaying the diameter of  $\text{CeO}_2$  nanoparticles, is shown in Figure S1). The shape and size of ceria nanoparticle is reported to increase with increasing molar ratio of the alkali used [51]. The dodecahedral morphology

of pure phase ZIF-67 (Figure 2b) is clearly visible, with the particle size ranging from 400–500 nm. According to the literature, methyl-imidazole should always be used in excess to cobalt nitrate. This is because it acts not only as an organic linker during the synthesis, but also as a stabilizing agent in its neutral form, which is advantageous for fabricating uniform dodecahedral particles of ZIF-67 [54]. After synthesizing the pure phase ZIF-67 crystals and CeO<sub>2</sub> nanoparticles, the same CeO<sub>2</sub> nanoparticles were dispersed in methanol through an ultrasound treatment followed by the addition of methylimidazole and cobalt nitrate, as explained in the experimental section, to form the inserted hybrid nanostructures. Figure 2c,d shows the SEM images of the ZIF-6/CeO<sub>2</sub> hybrid. Small ceria nanoparticles are seen to be mounted on the surface of the ZIF-67 polyhedrons. The polyhedrons range in the size of 450 nm and are uniformly distributed. Figure 2e presents the morphology analysis of Cu doped CeO<sub>2</sub> nanoparticles. The average particle size from the SEM image is found to be 30–40 nm. From the literature, the addition of Cu content into ceria tends to influence its crystallization process with the increase in the surface area of the resulting product and a smaller crystallite size than pure ceria [52]. It demonstrates the function of Cu in the growth process of ceria nanospheres. Figure 2f shows the morphology of 90 mol% Cu<sup>2+</sup> doped in CeO<sub>2</sub> nanoparticles. Polyhedral particles of Cu<sub>2</sub>O in the size range of 150–170 nm can be observed.

Transmission Electron Microscopy (TEM) was used to investigate the microstructure analysis of the prepared hybrids. Figure 3 presents the TEM imaging for ZIF-67/CeO<sub>2</sub> hybrids.

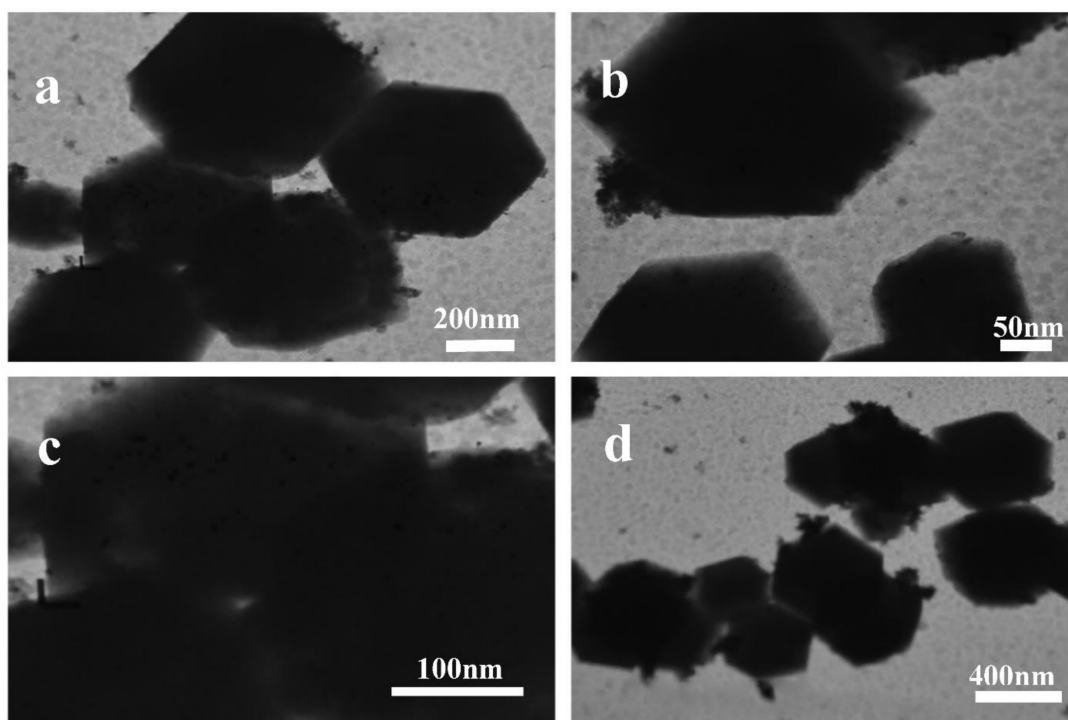


**Figure 3.** TEM images of ZIF-67/CeO<sub>2</sub> nano hybrids; (a) 200 nm, (b) 50 nm, (c) 100 nm, (d) 400 nm.

The TEM images clearly display the dodecahedral morphology of ZIF-67 particles. Interestingly, the enlarged TEM image (Figure 3c) validates the partial incorporation of CeO<sub>2</sub> nanoparticles inside ZIF-67, and these can also be seen to be attached/mounted onto the surface of larger particles of ZIF-67. The CeO<sub>2</sub> nanoparticles were measured as 30–40 nm in size (Figure S2). The fabrication process for such unique hybrids is presumed to occur by the pre-mixing of CeO<sub>2</sub> nanoparticles and methyl-imidazole molecules that makes the methyl-imidazole molecules to correlate with Ce ions on the surface of CeO<sub>2</sub> nanoparticles. Further, the surface nucleation of ZIF-67 crystals occurs by adding Co<sup>2+</sup> into the reaction mixture. However, some of the CeO<sub>2</sub> nanoparticles become mounted on the

surface of ZIF-67 crystals while some of them become embedded inside the polyhedral structure of ZIF-67. Additionally, the fast growth rate of ZIF-67 resulted in the successful incorporation of the as-synthesized CeO<sub>2</sub> nanoparticles into ZIF-67 crystals [24]. From these results, we can say that the on-site self-embedded growth behavior and surface nucleation makes these ingredients become firmly coupled together, and this is also a facile technique that does not make use of any additional agent. Figure S3a,b presents the TEM images of pure ZIF-67 and CeO<sub>2</sub> nanoparticles, respectively, while Figure S3c gives the HRTEM (SAED (selected area electron diffraction)) pattern of the hybrid nanostructure. It can be seen clearly that polycrystalline CeO<sub>2</sub> is partially embedded in ZIF-67, as there are diffused rings in the SAED pattern, whereas CeO<sub>2</sub> particles are also dispersed on the surface of ZIF-67 (Figure S3d).

Figure S4 shows the EDS (energy dispersive spectroscopy) spectrums obtained for ZIF-67/CeO<sub>2</sub> hybrid and Cu doped CeO<sub>2</sub>. For ZIF-67/CeO<sub>2</sub> in Figure S4a, it is demonstrated that the particles in the sample consisted of the elements Co, Ce, O, N, and C, supporting the presence of Ce along with Co, O, and N. Similarly, for the Cu doped structure no other impurity was detected, and the presence of Cu along with Ce and O confirmed the formation of a doped sample. FTIR (Fourier transform infrared spectroscopy) analysis of the as-synthesized samples was performed. Figure S5a,b shows the FTIR spectrum of pure CeO<sub>2</sub> and ZIF-67, whereas ZIF-67/CeO<sub>2</sub> is shown in Figure S5d. For pure ZIF-67, the strong peaks are obtained at 2925 cm<sup>-1</sup>, 1574 cm<sup>-1</sup>, 756 cm<sup>-1</sup>, and 424 cm<sup>-1</sup>. The peaks observed at 2925 and 2960 cm<sup>-1</sup> represent the C-H stretching vibrations of the -CH<sub>3</sub> group, while the one at 422 cm<sup>-1</sup> represents the Co-N stretching vibration. The peaks at 1574 cm<sup>-1</sup> and 756 cm<sup>-1</sup> correspond to the stretching as well as bending-mode vibrations of C=N, which is present in 2-methyl imidazole. The strong peaks around 1000 to 1500 cm<sup>-1</sup> represent the skeletal vibrations of the imidazole ring present in ZIF-67 [55]. This shows the phase purity of ZIF-67. For ZIF-67 embedded CeO<sub>2</sub>, there are no visible peaks present for Ce-O bond and all the peaks present display the formation of perfect ZIF-67 crystals. FTIR analysis of the synthesized samples of Cu doped CeO<sub>2</sub> is shown in the Figure S5c. Pure CeO<sub>2</sub> contains strong bands at 3399 cm<sup>-1</sup>, 1620 cm<sup>-1</sup>, and 540 cm<sup>-1</sup>. The broad bands at 3390 cm<sup>-1</sup> and 1620 cm<sup>-1</sup> correspond to the symmetric stretching and bending vibrations of physisorbed water molecules. Furthermore, the band at 540 cm<sup>-1</sup> shows the stretching-mode of the Ce-O bond [56]. For the Cu doped sample, stronger bands are obtained around 1600 to 1300 cm<sup>-1</sup>, which corresponds to the O-C-O stretching band. The peaks present around 700 cm<sup>-1</sup> display the Ce-O-C bending-mode vibrations: this is visible in both spectrums. The peak present at 500 cm<sup>-1</sup> in the doped sample shows the stretching vibration of the Ce-O bond and verifies the formation of cerium oxide without any impurities [57].

Figure 4a,b shows the TG/DTA (Thermogravimetric/Differential thermal analyzer) curves of pure CeO<sub>2</sub> and Cu doped CeO<sub>2</sub>, respectively. For pure CeO<sub>2</sub>, continuous weight loss is observed when it is heated from room temperature to 800 °C, which at first is due to the absorbed water molecules present in the sample. Further weight loss can be attributed to the decomposition of Ce(OH)<sub>3</sub> or Ce(OH)<sub>4</sub>/CeO<sub>2</sub>·2H<sub>2</sub>O, suggesting either a partially hydration (CeO<sub>2</sub>·nH<sub>2</sub>O) or a mixture (CeO<sub>2</sub> + CeO<sub>2</sub>·2H<sub>2</sub>O) of ceria phases. The DTA curve shows an exothermic peak at around 350 °C, corresponding to a weight loss, which must be considered a result of the crystallization of the residual amorphous phase. The total weight loss observed for the CeO<sub>2</sub> sample is almost 20%. For the Cu doped sample, the TGA curve shows continuous decomposition when it is being heated at room temperature until it becomes stable at 650 °C. The exothermic peak at around 250 °C, shown by the DTA curve, is an indication of the loss of the absorbed water molecules present in the sample. Although both the curves for pure CeO<sub>2</sub> and the doped sample (10% Cu) exhibit similar behavior altogether, there is a slight difference in the amount of weight loss at different temperatures, which can be clearly seen from the TGA graphs. The doping of CeO<sub>2</sub> with Cu causes it to be a better thermal conductor, and thus it loses more weight at extreme temperatures in comparison to pure CeO<sub>2</sub>.

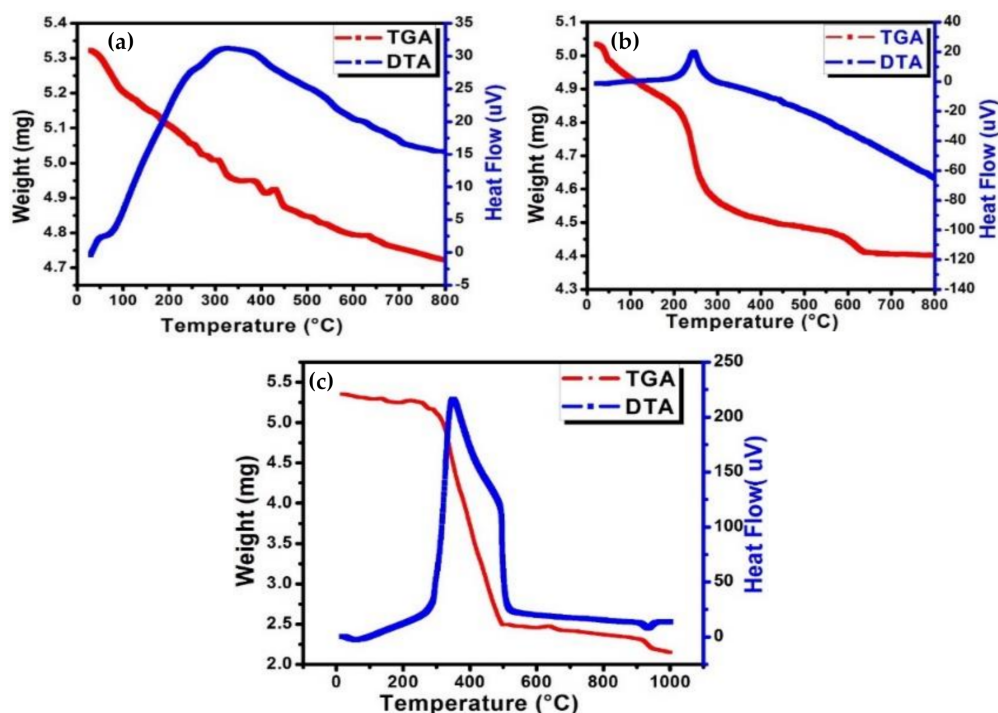


**Figure 4.** TG/DTA curves of (a) Pure CeO<sub>2</sub> (b) 10% Cu doped CeO<sub>2</sub> (c) ZIF-67/CeO<sub>2</sub> Nanohybrid.

Figure 4c shows the TG/DTA curve for the as-synthesized ZIF-67/CeO<sub>2</sub> hybrid in air atmosphere. It is demonstrated through the curve that ZIF-67/CeO<sub>2</sub> shows very little decomposition in the temperature range of 0 to 300 °C, which can be ascribed to the removal of absorbed water molecules or any unreacted 2-methylimidazole and solvents present in the sample. From the literature, it has been studied that ZIF-67 displays a higher thermal stability in vacuum than in air, illustrating its quite sensitive nature towards oxygen at extreme temperatures, although its stability still exceeds many other MOFs and metal oxides [42]. The sudden mass decomposition in the temperature range of 350–500 °C indicates that the Co/Ni metal–organic framework was converted to metal oxides with a corresponding exothermic peak, shown by the DTA curve, at approximately 400 °C. The mass remains almost unchanged at temperatures higher than 500 °C, suggesting that the organic components were completely removed and Co<sub>3</sub>O<sub>4</sub>/NiCo<sub>2</sub>O<sub>4</sub> composites were formed [58]. The presence of CeO<sub>2</sub> particles inside ZIF-67 do not seem to have any significant effect on the thermal stability of ZIF-67. At a temperature of 950 °C, the weight remains almost 10% of the original mass. The TGA curve matches well with the published data for pure ZIF-67. Furthermore, XPS (X-ray photoelectron spectroscopy) was performed for the surface compositional analysis and investigation of the chemical states of ZIF-67/CeO<sub>2</sub> sample.

Figure 5 shows the XPS spectrums that were obtained for ZIF-67/CeO<sub>2</sub>. After curve fitting, the binding energies on Ce 3d spectra conform to the Ce 3d<sub>3/2</sub> and Ce 3d<sub>5/2</sub> spin-orbit states as shown in Figure 5a. The peak at binding energy of 914.9 eV is a character of Ce (IV). In detail, the results obtained from the curve fitting show that the peaks at 880.2 eV, around 884 eV, 900 eV, and 904.0 eV are because of the emissions from Ce<sup>3+</sup>, while all the other peaks i.e., 886.0, 890, 896.3, 898.9 eV, are a result of emissions from Ce<sup>4+</sup>. The ratio of Ce<sup>3+</sup>/Ce<sup>4+</sup> can be semi-quantified based on the peak area. The presence of Ce<sup>3+</sup> may induce more oxygen vacancies and defects [14,59]. The binding energies 781.8 eV and 796.2 eV are attributed to Co 2p<sub>3/2</sub> and Co 2p<sub>1/2</sub>, respectively [60]. The satellite peak at around 786.3 eV is an aspect of Co (II), showing the presence of Co (II) in the product [61]. The O 1s peak is deconvoluted into three peaks. The binding energy at 529.5 eV is ascribed to the lattice oxygen of CeO<sub>2</sub>, and the one at 531.6 eV can be ascribed to hydroxyl species, defective oxygen and absorbed oxygen [62,63]. The peak at 533 eV is attributed to absorbed

water molecules [64]. XPS signals take into account the chemical state of the surface atoms, and the strong peak at 531.6 eV suggests that there are a lot of surface hydroxyls in the product and the presence of  $\text{Ce}^{3+}$  would aid the raise of absorbed oxygen [65]. More precisely, the N1s speak (Figure 5d) is deconvoluted into three different N species: pyridinic N at 398.3 eV, graphitic N at 398.8 eV. Among them, major species is the pyridinic N that is known to be more active than other N species [66]. The high-resolution spectrum of C 1s (Figure 5e) is fitted by three peaks at 281.9, 282.4 and 284.8 eV corresponding to C-C, C=C, and C=N/C-O. These functional groups arise from the decomposition of organic frameworks and notably affect the electronic structure/binding affinity of carbon materials [67].

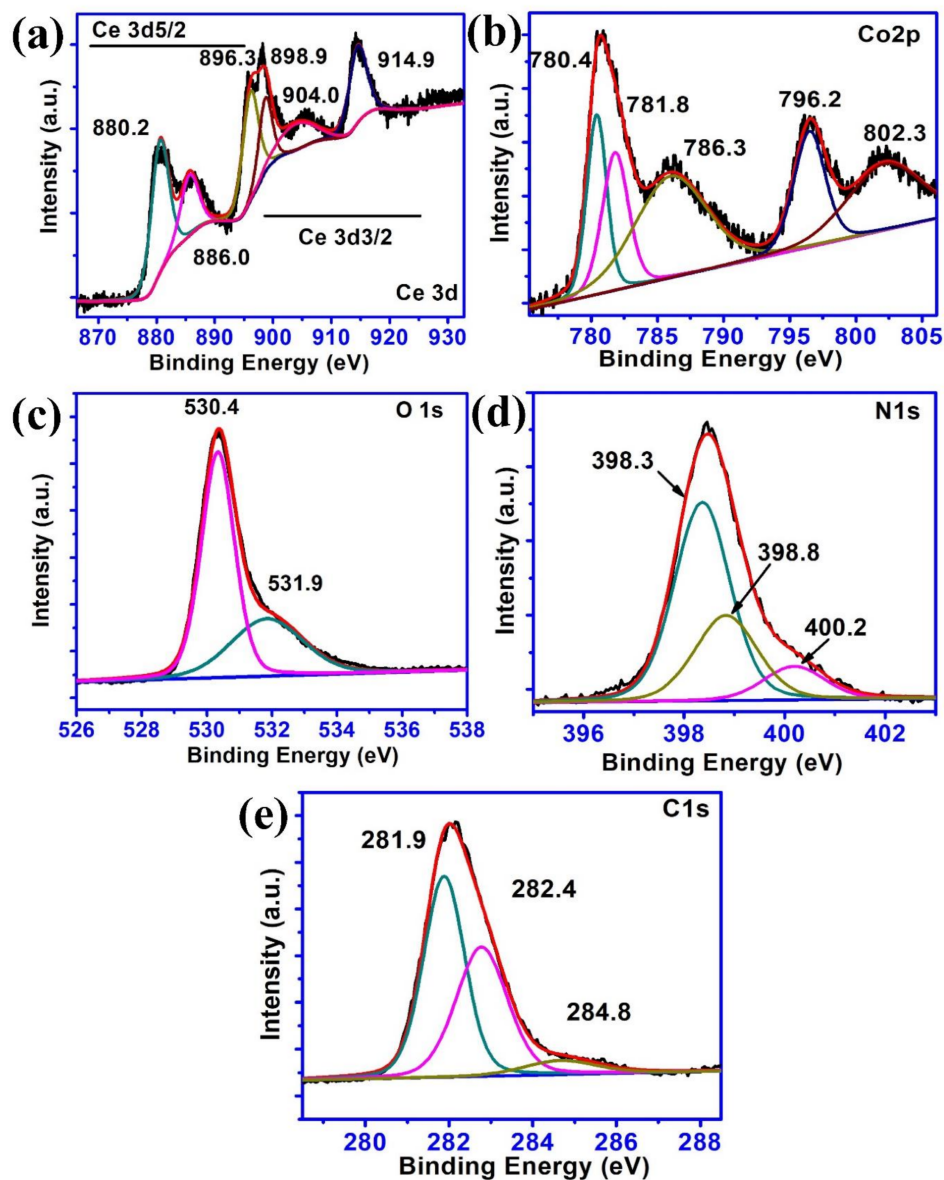


Figure 5. The XPS spectra of ZIF-67/CeO<sub>2</sub> (a) Ce 3d (b) Co 2p (c) O 1s (d) N1s (e) C 1s.

The porosity and specific surface area of the samples which can affect catalytic performance were carefully examined by nitrogen adsorption–desorption isotherm measurements for ZIF-67 and CeO<sub>2</sub> as shown in Figure 6.

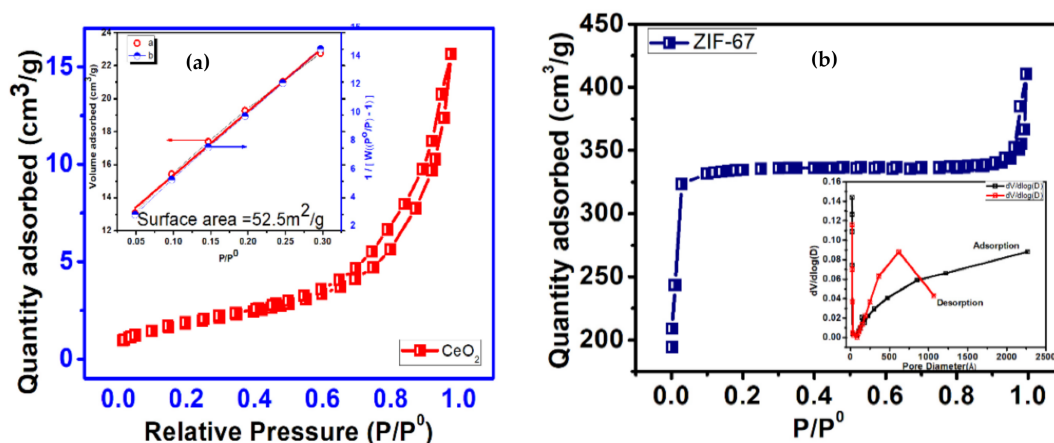


Figure 6. N<sub>2</sub> adsorption–desorption isotherms of (a) Pure CeO<sub>2</sub>, and (b) ZIF-67.

The N<sub>2</sub> adsorption–desorption isotherms for CeO<sub>2</sub> nanoparticles exhibits a type-II adsorption curve reflecting a non-porous character [14]. It is in accordance with the previously published reports. The calculated BET (Brunauer-Emmett-Teller) surface area of CeO<sub>2</sub> nanoparticles is 52.5 m<sup>2</sup>/g. For ZIF-67 polyhedrons, a type-I N<sub>2</sub> adsorption–desorption without hysteresis was obtained, which reflects its microporous nature [53]. Its surface area was measured to be 1085 m<sup>2</sup>/g. The pore size distribution of ZIF-67 is also shown where it can be seen that pores with smaller diameter have a larger density in comparison to the pores with larger diameter.

Figure 7 shows the NH<sub>3</sub>-TPD (Temperature-programmed Desorption) results obtained for pure ZIF-67, CeO<sub>2</sub> and hybrid ZIF-67/CeO<sub>2</sub> nanostructures.

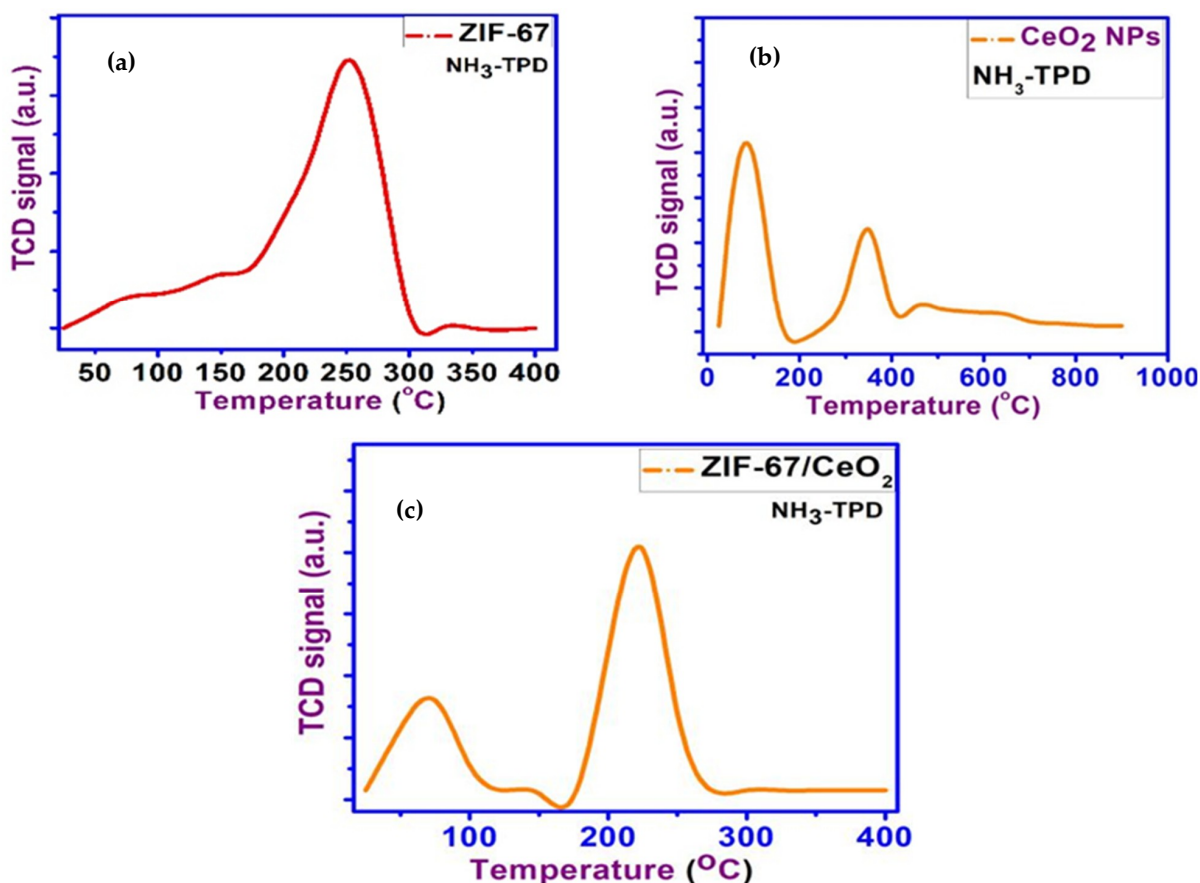


Figure 7. NH<sub>3</sub>-TPD results of (a) ZIF-67, (b) CeO<sub>2</sub> and (c) ZIF-67/CeO<sub>2</sub>.

TPD was performed to find out the acidic and basic sites present in the catalyst. For ZIF-67, according to the literature it is known that the acidity of ZIF-67 originates from Co (II) and Co (III) species and the basic sites result from N atoms of imidazole ligand present on its surface [68]. The  $\text{NH}_3$ -TPD curve for ZIF-67 (Figure 7a) shows a desorption peak obtained at around 250 °C. This shows the moderate acidic strength of ZIF-67 to be used as an active catalyst. For  $\text{CeO}_2$ , two desorption peaks are obtained (Figure 7b); one at the lower temperature of 100 °C, which is attributed to the weak acidic sites with a greater peak area [69]. The peak at the higher temperature of 300 °C shows the presence of moderately strong acidic sites on  $\text{CeO}_2$  surface. Figure 7c shows the desorption peaks for the composite sample ZIF-67/ $\text{CeO}_2$ , where less density of weak acidic sites and larger concentration of moderately strong acid sites can be observed owing to formation of q hybrid structure having the synergistic impact of ZIF-67 and  $\text{CeO}_2$ , which results in the creation of greater acidic sites on the catalyst surface.  $\text{H}_2$ -TPR (Temperature-Programmed Reduction) analysis was performed to analyze the reductive behavior of the prepared samples. Figure 8 shows the TPR result of ZIF-67/ $\text{CeO}_2$  and the inset compares  $\text{H}_2$ -TPR to pure  $\text{CeO}_2$ .

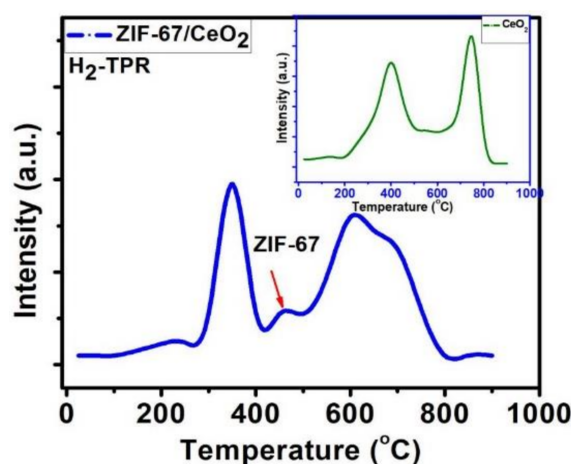


Figure 8.  $\text{H}_2$ -TPR results of  $\text{CeO}_2$  and ZIF-67/ $\text{CeO}_2$ .

It can be observed that the pure  $\text{CeO}_2$  TPR profile consists of two peaks, one at the lower temperature of 400 °C and the second peak at around 800 °C. The lower temperature peak can be ascribed to the capping oxygen present at the surface of ceria, whereas the high temperature peak is due to the bulk oxygen present in the sample. These oxygen species are responsible for hydrogen uptake in the  $\text{H}_2$ -TPR analysis [14,70]. For the hybrid ZIF-67/ $\text{CeO}_2$  sample, three peaks were obtained. The peak around 350 °C is the characteristic peak of ceria which is now shifted to lower temperature as compared to pure ceria. The peak around 500 °C is characteristic of ZIF-67, which is ascribed to the presence of N-species present on its surface and are responsible of hydrogen uptake [68]. The second characteristic peak of ceria is also shifted to a lower temperature; it is now at 600 °C with a larger peak area, as compared to pure ceria where it was at 800 °C. This can be explained by the synergistic properties obtained by the formation of a hybrid structure which increases the reducibility and hence the catalytic activity of the catalyst.

#### Catalytic Activity

To investigate the catalytic activity of ZIF-67/ $\text{CeO}_2$ , and Cu doped  $\text{CeO}_2$  nanostructures, solvent-free oxidation of cyclohexene was carried out with  $\text{H}_2\text{O}_2$  to produce adipic acid.  $\text{H}_2\text{O}_2$  is a green oxidant as it produces water as the only by-product and is a preferable choice for a sustainable and environmental friendly process [71]. The amount of the catalyst ZIF-67/ $\text{CeO}_2$  taken was varied from 0.5 g to 1.5 g. The optimum amount of ZIF-67/ $\text{CeO}_2$  hybrid obtained was 1.2 g, with a maximum yield (72%) of adipic acid as per the weight of the white crystalline solid obtained after cooling it down in an ice bath. To confirm

the formation of pure phase adipic acid, FTIR analysis was performed. Figure 9 shows the FTIR spectrum of obtained adipic acid. It displays the strong characteristic peak at  $1685\text{ cm}^{-1}$ , which is ascribed to the stretching vibrations of carboxylic groups present in AA [72]. The peak at  $2981\text{ cm}^{-1}$  displays the C-H stretching present in its structure. Other than that, a few peaks after 1000 (at approximately  $1150$  and  $1300\text{ cm}^{-1}$ ) correspond to C-O stretching vibrations.

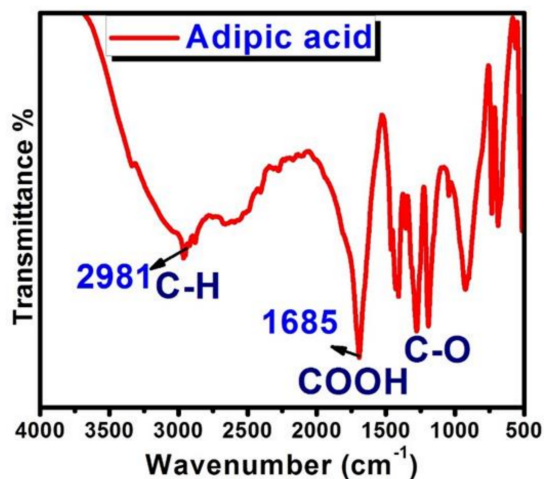


Figure 9. FTIR spectrum of synthesized adipic acid.

These results match well with the previously reported work and demonstrate the formation of pure phase adipic acid. The catalytic activity of Cu-doped  $\text{CeO}_2$  and pure  $\text{CeO}_2$  nanospheres were also tested under the same reaction conditions, but no conversion of cyclohexene was observed for a variable range of catalyst amounts. This confirms that metal doped ceria particles have shown no catalytic activity in the production of adipic acid and the role of ZIF-67 is critical in the catalytic activity of hybrid nanostructures.

The reaction mechanism for the oxidative cleavage of cyclohexene passes through several oxidation and hydrolysis steps. The oxidation of cyclohexene by  $\text{H}_2\text{O}_2$  generally includes epoxidation of the double bond present in cyclohexene, followed by a fast hydrolytic ring opening of the bicyclic epoxide and conversion to a diol, dehydrogenation of the secondary alcohol, the formation of hemi-acylal, then a Baeyer–Villiger oxidation and multiple hydrolysis steps resulting in adipic acid [71,73–75]. ZIF-67 has been previously used for several organic transformations but not for this particular reaction where the oxidation of cyclohexene takes place in the presence of  $\text{H}_2\text{O}_2$ . It was suggested that as ZIFs are saturated metal organic frameworks and are theoretically free of low coordinated metal atoms and functionalized linkers other than metal centers, so they should not be capable of displaying any catalytic activity [20]. On the other hand, Chizallet et al. reported a thorough study using the DFT (Density functional theory) theory to calculate the strength of Lewis acid-base sites, the structural defects and low coordinated acid-base species that coexist on the surface of the framework and are accountable for the catalytic ability [76]. The presence of acido-basic sites on the external surface of ZIF-67 are mainly responsible for its catalytic activity and their presence is analyzed by the  $\text{NH}_3$ -TPD results previously discussed. These species may include OH and NH groups, hydrogen carbonates, low-coordinated Co atoms, and free N- moieties belonging to the linkers [68,77]. The proportion of low coordinated Co atoms such as Co III nodes and Co II nodes depends on the number of linkers lost around the exposed Co center [68]. The presence of small amounts of atmospheric moisture may lead to the formation of NH, -OH and hydrogen carbonate species on the ZIF surface, which accelerates the epoxides system (Figure 10). On the other hand, the presence of  $\text{CeO}_2$  has its own role in the catalytic activity of this reaction. Ceria has the ability of transfer between two oxidation states i.e.,  $\text{Ce}^{3+}$  and  $\text{Ce}^{4+}$  and its catalytic activity is known to depend on this redox cycle of  $\text{Ce}^{4+}/\text{Ce}^{3+}$  [78]. Furthermore, ceria

has been reported to decompose  $\text{H}_2\text{O}_2$  to produce molecular oxygen and the hydrogen radical along with the  $\text{Ce}^{4+}/\text{Ce}^{3+}$  cycle. However, the amount of  $\text{H}_2\text{O}_2$  plays a key role in maintaining the redox cycle of Ce in  $\text{CeO}_2$ . The redox cycle of Ce in  $\text{CeO}_2$  i.e., the catalytic activity of  $\text{CeO}_2$ , is reported to be inhibited by incorporating a higher amount (exceeding 0.2 M) of  $\text{H}_2\text{O}_2$ . Herein, 0.1 M of  $\text{H}_2\text{O}_2$  is employed to ensure maximum catalytic activity of the catalyst. Furthermore, in previous reports the adsorption of organic compounds on  $\text{CeO}_2$  particles is suggested to be a completely surface-localized reaction, with  $\text{Ce}^{3+}$  and molecular oxygen being the active sites on its surface [79,80]. The incorporation of  $\text{CeO}_2$  nanoparticles into polyhedral ZIF-67 reduces the agglomeration of  $\text{CeO}_2$  nanoparticles as shown by the TEM images in Figure 3, consequently increasing the catalytic activity of  $\text{CeO}_2$ . Based on the above information, a proposed mechanism is presented in Figure 11, which is based on the presence of active sites on the catalyst surface.

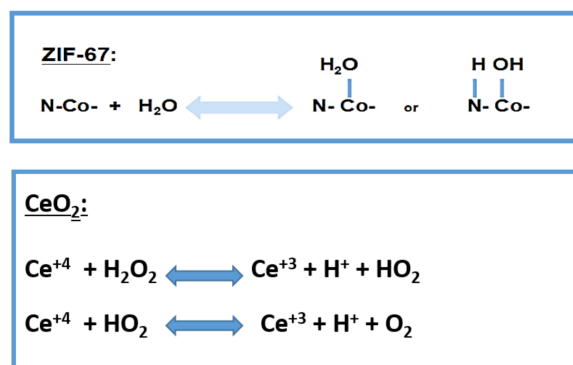


Figure 10. Active species formation on the surface of ZIF-67/ $\text{CeO}_2$ .

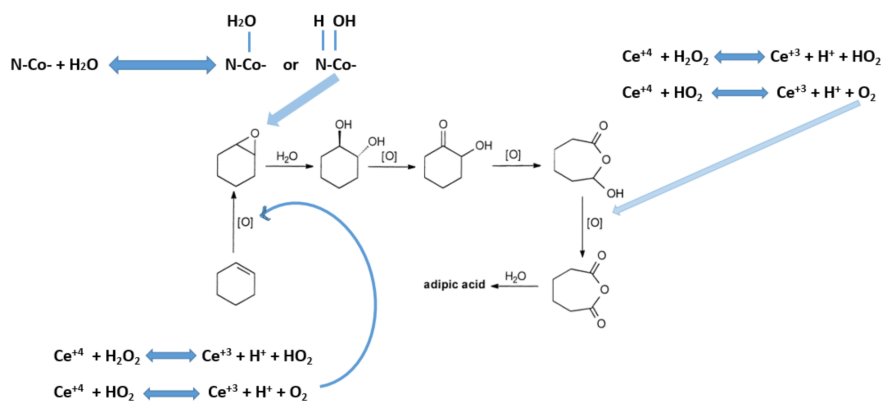


Figure 11. The reaction mechanism for the oxidation of cyclohexene with ZIF-67/ $\text{CeO}_2$  as a catalyst.

The first stage in the formation of adipic acid is the epoxidation of cyclohexene, which afterwards goes through hydrolysis to form cyclohexane diol. The diol can then be transformed into adipic acid because of the oxidative cleavage of the C-C bond. Epoxidation of cyclohexene has been reported as the rate determining step (RDS) in the formation of adipic acid, while all other steps take place very fast [45]. The epoxide formation of cyclohexene is accelerated by the rapid decomposition of  $\text{H}_2\text{O}_2$  by Ce ions present on the ceria surface, which produces more O atoms for the epoxide reaction to take place fast, and is presumed from the work of Wandong et al. [80]. The Raman results in their previous work also suggested the appearance of molecular oxygen and peroxide-like species ( $\text{O}_2^{2-}$ ) on the surface of  $\text{CeO}_2$  after reaction with  $\text{H}_2\text{O}_2$ , which supports our proposed mechanism. Secondly, the ring opening of epoxide is proposed to be accelerated by the presence of Co centers on ZIF surface [81]. Park et al. suggested the idea that the crystal plane of Co-Im-Zn is the active surface for the epoxide activation, rather than single uncoordinated

metal atoms [82]. Regardless, it is generally accepted that the metal center present in ZIFs coordinates the oxygen of the epoxide to achieve ring opening by weakening the  $\beta$  C-O bond [68,83]. Therefore, it was presumed that it bonds with oxygen to form CoO or Co<sub>2</sub>O<sub>3</sub> compounds and causes the ring opening of epoxide to form a diol. Further dehydrogenation and hydrolysis steps, involved in the production of adipic, are proposed to be taken rapidly through the presence of active sites on the catalyst's surface. The synergistic effect of the synthesized catalyst ZIF-67/CeO<sub>2</sub> can be explained through the reported work of Fang et al. [84]. A higher surface charge ratio was observed in the case of CeO<sub>2</sub>@Co<sub>3</sub>O<sub>4</sub> (Co<sup>3+</sup>/Co<sup>2+</sup> and Ce<sup>3+</sup>/Ce<sup>4+</sup>) through XPS measurements, which led to a larger amount of oxygen vacancies and hence better catalytic activity. The surface chemical states of the synthesized CeO<sub>2</sub> and Co based catalyst were also studied, where the values of Ce<sup>3+</sup>/Ce<sup>4+</sup> and Co<sup>3+</sup>/Co<sup>2+</sup> showed a slight decline after the reaction, which suggested the existence of a synergistic effect between Co and Ce ions through the following redox equilibrium of Co<sup>2+</sup> + Ce<sup>4+</sup>  $\leftrightarrow$  Co<sup>3+</sup> + Ce<sup>3+</sup> during the oxidation reaction [85]. In addition to that, TPR results presented by Fang et al. suggested an increased reducibility for their combined Ce and Co catalyst, indicating a strong synergistic effect between the cobalt and cerium ions present in our catalyst [84]. Apart from that, a high BET surface area of ZIF-67/CeO<sub>2</sub> is supposed to play a significant role in the oxidation of cyclohexene, because a high surface area catalyst is reported to provide a greater number of active surface sites to promote the oxidation of cyclohexene molecules, resulting in high conversion of cyclohexene molecules [86]. Furthermore, the porous nature of ZIF-67 is expected to provide enhanced mass transport into the interior of the catalyst [87].

For the ZIF-67/CeO<sub>2</sub> sample, the formation of adipic acid takes place in less reaction time and at a lower temperature. Furthermore, the yield of adipic acid obtained after the oxidation of cyclohexene is said to be dependent on various factors, like the amount of reactants used, reaction time, and temperature etc. [45,74]. Keeping that in mind, an optimum set of conditions are applied in our study to ensure satisfactory results. Ordinarily, 4 moles of H<sub>2</sub>O<sub>2</sub> are theoretically needed for the conversion of cyclohexene to adipic acid. However, 4.4 moles of H<sub>2</sub>O<sub>2</sub> were used in this research to assure the complete conversion of cyclohexene. Furthermore, a stepwise addition of H<sub>2</sub>O<sub>2</sub> is applied in this reaction which has already been investigated to increase the yield of adipic acid [45]. Altogether, a rather mild set of conditions are applied (90 °C, 12 h) for the conversion of cyclohexene into adipic acid in solvent-free conditions and an adequate yield of adipic acid is obtained. The catalytic activity of ZIF-67/CeO<sub>2</sub>, in the production of adipic acid, can also be compared to some of the previously employed catalysts as shown in Table 1. ZIF-67/CeO<sub>2</sub> is able to produce a comparable high yield of adipic acid (72%) with an adequate amount of catalyst used, and without the use of any solvent reagent to activate the oxidant. Additionally, it can be synthesized through a facile one-step procedure at ambient conditions.

**Table 1.** Comparison of this work with other reported catalysts producing adipic acid through oxidation of cyclohexene.

Catalysts	Yield (%) <sup>a</sup>	Reaction Conditions	Reactant Conversion (%) <sup>b</sup>	Product Selectivity (%) <sup>c</sup>	Reference
MIL-101	90	70 °C, 8 h	>99	Not reported	[45]
WO <sub>4</sub> /silica gel	84	87 °C, 15 h	100	99	[74]
Ag <sub>2</sub> WO <sub>4</sub>	85	75 °C, 18 h	99	98	[73]
Cu/WO <sub>3</sub>	66	70 °C, 12 h	75	88	[88]
K <sub>3</sub> PW <sub>12</sub> O <sub>40</sub>	77	75 °C, 24 h	100	Not reported	[89]
Na <sub>2</sub> WO <sub>4</sub>	80	85 °C, 8 h	>99	Not reported	[90]
ZIF-67/CeO <sub>2</sub>	72	90 °C, 12 h	100%	>99%	This work

<sup>a</sup> The yield refers to the pure product of adipic acid produced in each of these reactions, <sup>b</sup> Cyclohexene is the reactant used for all the catalysts shown in the table. This shows the percentage conversion of cyclohexene for each respective reaction. <sup>c</sup> Selectivity of adipic acid is presented in percentage for each reaction mentioned in the table.

In summary, this mechanism has high oxygen storage capacity and redox properties of CeO<sub>2</sub> (couples of Ce<sup>4+</sup>/Ce<sup>3+</sup>), which produces lots of active oxygen available for the

oxidation process [91]. This coupled with the microporous nature of ZIF-67 provided the basis of an effective catalyst to produce adipic acid. Such a facile and cost-effective strategy can result in self-inserted hybrid structures with high specific surface areas that are firmly coupled together.

### 3. Methods and Materials

#### 3.1. Synthesis of CeO<sub>2</sub> Nanoparticles

The synthetic process of ceria nanoparticles is in accordance with the report published by Lin's group [51]. Typically, 0.9 g of PVP (polyvinyl pyrrolidone) and 0.434 g of cerium nitrate hexahydrate (Ce (NO<sub>3</sub>)<sub>3</sub>·6H<sub>2</sub>O) were both dissolved in 30 mL of DI (deionized water) water. After some time, 0.04 g of NaOH was added into the solution and stirred for 30 min at room temperature. After that, the prepared solution was transferred into a Teflon-lined 75 mL autoclave. The autoclave was put in the oven at a temperature of 180 °C for 24 h. The resulted precipitates were collected by centrifugation and washed thrice with ethanol and DI water. It was finally dried in an oven at 80 °C for 2 h.

#### 3.2. Synthesis of ZIF-67 and ZIF-67/CeO<sub>2</sub>

Typically, 20 mg of the as-prepared CeO<sub>2</sub> nanoparticles were dispersed under ultrasonication in 20 mL absolute methanol. Under vigorous stirring, 328 mg of 2-methyl imidazole powder is added in that solution. After half an hour, 5 mL of cobalt nitrate Co (NO<sub>3</sub>)<sub>2</sub> methanol solution (291 mg in 5 mL of methanol) was poured into the mixture. This mixture was aged for 3 days under ambient conditions. Finally, the precipitates were collected by centrifugation and washed with methanol and dried for its application. Pure ZIF-67 was also prepared by the same method without the addition of CeO<sub>2</sub> nanoparticles.

#### 3.3. Synthesis of Cu Doped CeO<sub>2</sub> Nanospheres (10% vs. 90%)

This synthesis is in accordance with the report published by Yang. For 10% Cu, 117.0 mg (0.27 mmol) of (Ce (NO<sub>3</sub>)<sub>3</sub>·6H<sub>2</sub>O) and 200 mg of PVP were dissolved in 19 mL of DI water. This was followed by the addition of 0.9 mL of Cu (NO<sub>3</sub>)<sub>2</sub>·3H<sub>2</sub>O (5 g L<sup>-1</sup>) and 0.1 mL of H<sub>2</sub>O<sub>2</sub> under vigorous stirring for 30 min. The as-prepared transparent solution was transferred into a 50 mL Teflon-lined autoclave and heated for 5 h at 180 °C. The resulting precipitates were collected by centrifugation, followed by washing three times with ethanol. Finally, the dried product was obtained by heating in an oven for 6 h at 70 °C [52]. The same method was repeated for 90% Cu by varying the molar ratio of cerium and copper precursor.

#### 3.4. Oxidation of Cyclohexene with H<sub>2</sub>O<sub>2</sub>

For this part of the experiment, we used cyclohexene (25 g), H<sub>2</sub>O<sub>2</sub> (150 mL) and a catalyst 1.2 g. A 250 mL flask equipped with a reflux condenser and a temperature sensor was taken. For this purpose, 1.2 g of the ZIF-67/CeO<sub>2</sub> catalyst was taken in the flask along with cyclohexene and heated up to 40 °C with a stepwise addition of H<sub>2</sub>O<sub>2</sub> and stirred at this temperature for 30 min. Further heating was done to 90 °C for 12 h. At the end of reaction, the slurry was cooled to room temperature and then placed at 4 °C overnight. The resulting solid was collected via vacuum filtration and washed with a small portion of cold water and dried to afford pure adipic acid in 72% yield.

The conversion of cyclohexene, selectivity and yield to adipic acid were calculated according to the following expressions:

$$\text{Conversion} = (\text{mols of cyclohexene reacted} / \text{mols of cyclohexene initial}) \times 100$$

$$\text{Selectivity} = (\text{mols of desired product} / \text{sum of mols of all products}) \times 100$$

$$\text{Yield} = (\text{actual yield of adipic acid} / \text{theoretical yield of adipic acid}) \times 100$$

#### 3.5. Characterization Techniques

The structural analysis of materials was performed using powder X-ray Diffraction on a STOE Theta/theta X-ray Diffractometer System (STOE, Darmstadt, Germany) with an op-

erating voltage and current of 40 kV and 40 mA, respectively, using monochromatic Cu K $\alpha$  radiation ( $\lambda = 0.15418$  nm). The particles' morphology was investigated by a Field Emission Scanning Electron Microscopy (FESEM) instrument (VEGA3 TESCAN, Brno, Czech Republic). JEM-2100 model Transmission Electron Microscopy (TEM) (Hitachi, Tokyo, Japan) was used to investigate the microstructure and hybrid formation. Binding energy analysis of prepared hybrids was done using ESCALAB250Xi (XPS) (ThermoFisher Scientific, Waltham, MA, USA) with Al K $\alpha$  (1486.6 eV) X-rays as the excitation basis and C1s (284.5 eV) was selected as the reference. Pore size (BJH) information and available specific surface area (multipoint (Brunauer–Emmet–Teller (BET)) of prepared hybrids was calculated using N<sub>2</sub> adsorption desorption on Porosimetry System (ASAP 2420; Micromeritics Instrument Corporation, Norcross, GA, USA) at a standard temperature of 77 K. Before the actual gas analysis, samples were outgassed under vacuum at 150 °C for 10 h. Adsorption data in the partial pressure ( $P/P_0$ ) range of 0.05–0.3 were used for the calculation. A Model (2910) Micromeritics Autochem with a thermal conductivity detector (TCD) was employed for H<sub>2</sub> Temperature-programmed reduction (TPR) study. After pretreatment of the catalyst with 5 vol% O<sub>2</sub> in He at 500 °C for 1 h, 5% *v/v* of H<sub>2</sub> in Ar was flowed over the catalyst (200 mg) with a flow rate of 50 mL/min and a heating rate of 5 °C/min till 1000 °C. The same model was used to study Temperature-programmed desorption (TPD) behavior using ammonia (NH<sub>3</sub>), where desorbed NH<sub>3</sub> was monitored using the TCD signal and a mass spectrometer. The catalyst (200 mg) was taken and pre-treated with He at 200 °C for 30 min followed by ammonia adsorption for 1 h using 5 vol% NH<sub>3</sub> in He (50 mL/min). The physically adsorbed ammonia was purged using a flow of He (50 mL/min) for 30 min at 100 °C and cooled down to room temperature, followed by heating up till 500 °C (5 °C/min) under He flow for 60 min. NH<sub>3</sub>-TPD for pure CeO<sub>2</sub> particles was carried out till 900 °C (5 °C/min).

#### 4. Conclusions

In conclusion, the catalytic activity of CeO<sub>2</sub> nanoparticles has been evaluated with two different formulations: one was embedded into MOF (ZIF-67) and the second with Cu doped CeO<sub>2</sub> nanoparticles. This very facile and cost-effective approach was adopted to synthesize a hybrid structure of pure phase CeO<sub>2</sub> nanoparticles encapsulated inside ZIF-67 polyhedrons. The SEM and TEM results displayed CeO<sub>2</sub> nanoparticles mounted on the surface as well as embedded inside the ZIF-67 mesoporous structure. Both prepared nanostructures were used as catalysts for the rapid synthesis of adipic acid from oxidation of cyclohexene, and 72% yield was obtained in 12 h by ZIF-67/CeO<sub>2</sub> hybrids. Cu doped CeO<sub>2</sub> did not show any considerable activity for the production of adipic acid through the oxidation of cyclohexene. The as-prepared CeO<sub>2</sub>/ZIF-67 hybrid have the advantage of the microporous and molecular sieving manner depicted by the MOF matrix combined with the effective functional characteristics of cerium oxide nanoparticles. The fabrication procedure is suitable for an extensive range of metal/metal oxide nanoparticles, as it enables the encapsulation of multiple nanoparticles in an un-agglomerated fashion and can control the dimensional arrangement of nanoparticles inside the MOF array. Furthermore, ZIF-67, being highly porous, offers less diffusional resistance and thus increases catalytic activity. Therefore, large surface area ZIF-67/CeO<sub>2</sub> hybrids as heterogeneous catalysts were found to be a reasonable substitute to the supported or unsupported noble metal catalysts used to produce adipic acid through the oxidation of cyclohexene.

**Supplementary Materials:** The following are available online at <https://www.mdpi.com/2073-4344/11/3/304/s1>, Figure S1: SEM image of CeO<sub>2</sub> nanoparticles with diameters, Figure S2: SEM image of ZIF-67/CeO<sub>2</sub> with particle size, Figure S3: TEM images of (a) Pure ZIF-67 (b) Pure CeO<sub>2</sub> Nanoparticles (c) HRTEM (SAED) Pattern of ZIF-67/CeO<sub>2</sub> Nanohybrids (d) Low Resolution TEM of ZIF-67/CeO<sub>2</sub> Nanohybrids, Figure S4: EDS spectrums (a) ZIF-67/CeO<sub>2</sub> (b) Cu doped CeO<sub>2</sub>, Figure S5: FTIR spectrum of (a) Pure CeO<sub>2</sub> (b) Pure ZIF-67 (c) 10% Cu doped CeO<sub>2</sub> (d) ZIF-67/CeO<sub>2</sub> Nanohybrids.

**Author Contributions:** E.P. has helped conceiving and presenting the idea. S.B. has carried out the experiments and wrote the manuscript with support from O.R. and under the supervision of E.P. M.Y.

has encouraged and helped some analytical aspects of this work. All authors discussed the results and contributed to the final manuscript. All authors have read and agreed to the published version of the manuscript.

**Funding:** This research was funded by Higher Education Commission, Pakistan: 2017/HEC/NRPU/10482.

**Data Availability Statement:** No new data were created or analyzed in this study. Data sharing is not applicable to this article.

**Acknowledgments:** This work is supported by National University of Sciences and Technology (NUST) Pakistan and Higher Education Commission (HEC) Pakistan (2017/HEC/NRPU/10482). Author Minghui Yang would like to acknowledge Key Program of the Chinese Academy of Sciences (Grant No. KFZD-SW-320) and Natural Science Foundation of China (Grant No. 21471147). M.Y. would like to thank for the Ningbo 3315 program.

**Conflicts of Interest:** The authors declare no conflict of interest.

## References

1. Wang, F.; Liu, X. Recent advances in the chemistry of lanthanide-doped upconversion nanocrystals. *Chem. Soc. Rev.* **2009**, *38*, 976–989. [\[CrossRef\]](#)
2. Wang, J.; Wang, P.; Zhao, Q.; Yu, T.; Du, X.; Hao, X. Highly dispersed Ag nanoparticles embedded on the surface of CeO<sub>2</sub>/CF nanowires derived from three-dimensional structured Cu foam for toluene catalytic oxidation. *J. Mol. Catal.* **2020**, *486*, 110879. [\[CrossRef\]](#)
3. Nyk, M.; Kumar, R.; Ohulchansky, T.Y.; Bergey, E.J.; Prasad, P.N. High contrast in vitro and in vivo photoluminescence bioimaging using near infrared to near infrared up-conversion in Tm<sup>3+</sup> and Yb<sup>3+</sup> doped fluoride nanophosphors. *Nano Lett.* **2008**, *8*, 3834–3838. [\[CrossRef\]](#)
4. Hu, H.; Xiong, L.; Zhou, J.; Li, F.; Cao, T.; Huang, C. Multimodal-Luminescence Core–Shell Nanocomposites for Targeted Imaging of Tumor Cells. *Chem. Eur. J.* **2009**, *15*, 3577–3584. [\[CrossRef\]](#) [\[PubMed\]](#)
5. Weidenkaff, A.; Ebbinghaus, S.G.; Lippert, T. Ln<sub>1-x</sub>A<sub>x</sub>CoO<sub>3</sub> (Ln = Er, La; A = Ca, Sr)/Carbon Nanotube Composite Materials Applied for Rechargeable Zn/Air Batteries. *Chem. Mater.* **2002**, *14*, 1797–1805. [\[CrossRef\]](#)
6. Rajan, A.R.; Vilas, V.; Rajan, A.; John, A.; Philip, D. Synthesis of nanostructured CeO<sub>2</sub> by chemical and biogenic methods: Optical properties and bioactivity. *Ceram. Int.* **2020**, *46*, 14048–14055. [\[CrossRef\]](#)
7. Qi, J.; Zhao, K.; Li, J.; Gao, J.; Zhao, H.; Yu, R.; Tang, R. Multi-shelled CeO<sub>2</sub> hollow microspheres as superior photocatalysts for water oxidation. *Nanoscale* **2014**, *6*, 4072–4077. [\[CrossRef\]](#)
8. Yang, J.; Jia, Y.; Huang, B.; Li, X.; Guo, L.; Zheng, A.; Luque, R.; Sun, Y. Photoactive CeO<sub>2</sub>/SBA-15 functionalized materials as efficient systems for mono-dehydration of sugar alcohols. *Molecular Catalysis. J. Mol. Catal.* **2020**, *487*, 110844. [\[CrossRef\]](#)
9. You, Y.; Shi, C.; Chang, H.; Guo, L.; Xu, L.; Li, J. The promoting effects of amorphous CePO<sub>4</sub> species on phosphorus-doped CeO<sub>2</sub>/TiO<sub>2</sub> catalysts for selective catalytic reduction of NO<sub>x</sub> by NH<sub>3</sub>. *J. Mol. Catal.* **2018**, *453*, 47–54. [\[CrossRef\]](#)
10. Carrettin, S.; Concepción, P.; Corma, A.; López Nieto, J.M.L.; Puentes, V.F. Nanocrystalline CeO<sub>2</sub> increases the activity of Au for CO oxidation by two orders of magnitude. *Angew. Chem. Int. Ed.* **2004**, *43*, 2538–2540. [\[CrossRef\]](#)
11. Mai, H.X.; Sun, L.D.; Zhang, Y.W.; Si, R.; Feng, W.; Zheng, H.P.; Liu, H.C.; Yan, C.H. Shape-selective synthesis and oxygen storage behavior of ceria nanopolyhedra, nanorods, and nanocubes. *J. Phys. Chem. B* **2005**, *109*, 24380–24385. [\[CrossRef\]](#) [\[PubMed\]](#)
12. Nolan, M.; Parker, S.C.; Watson, G.W. The electronic structure of oxygen vacancy defects at the low index surfaces of ceria. *Surf. Sci.* **2005**, *595*, 223–232. [\[CrossRef\]](#)
13. Yu, X.; Wu, X.; Chen, Z.; Huang, Z.; Jing, G. Oxygen vacancy defect engineering in Mn-doped CeO<sub>2</sub> nanostructures for nitrogen oxides emission abatement. *J. Mol. Catal.* **2019**, *47*, 110512. [\[CrossRef\]](#)
14. Li, Z.; Han, F.; Li, C.; Jiao, X.; Chen, D. Hollow CeO<sub>2</sub> dodecahedrons: One-step template synthesis and enhanced catalytic performance. *RSC Adv.* **2016**, *6*, 60975–60982. [\[CrossRef\]](#)
15. Feng, Z.; Ren, Q.; Peng, R.; Mo, S.; Zhang, M.; Fu, M.; Chen, L.; Ye, D. Effect of CeO<sub>2</sub> morphologies on toluene catalytic combustion. *Catal. Today* **2019**, *332*, 177–182. [\[CrossRef\]](#)
16. Zhou, K.; Wang, X.; Sun, X.; Peng, Q.; Li, Y. Enhanced catalytic activity of ceria nanorods from well-defined reactive crystal planes. *J. Catal.* **2005**, *229*, 206–212. [\[CrossRef\]](#)
17. Alhumaimess, M.; Aldosari, O.; Alshammari, H.; Kamel, M.M.; Betiha, M.A.; Hassan, H.M.A. Ionic liquid green synthesis of CeO<sub>2</sub> nanorods and nano-cubes: Investigation of the shape dependent on catalytic performance. *J. Mol. Liq.* **2019**, *279*, 649–656. [\[CrossRef\]](#)
18. Tan, X.; Zhu, D.; Shi, Z.; Zhang, X. Thickness-dependent morphology, microstructure, adsorption and surface free energy of sputtered CeO<sub>2</sub> films. *Ceram. Int.* **2020**, *46*, 13925–13931. [\[CrossRef\]](#)
19. An, T.; Deng, X.; Liu, S.; Wang, S.; Ju, J.; Dou, C. Growth and roughness dependent wetting properties of CeO<sub>2</sub> films prepared by glancing angle deposition. *Ceram. Int.* **2018**, *44*, 9742–9745. [\[CrossRef\]](#)
20. Zanon, A.; Chaemchuen, S.; Mousavi, B.; Verpoot, F. 1 Zn-doped ZIF-67 as catalyst for the CO<sub>2</sub> fixation into cyclic carbonates. *J. CO<sub>2</sub> Util.* **2017**, *20*, 282–291. [\[CrossRef\]](#)

21. Yang, H.; He, X.W.; Wang, F.; Kang, Y.; Zhang, J. Doping copper into ZIF-67 for enhancing gas uptake capacity and visible-light-driven photocatalytic degradation of organic dye. *J. Mater. Chem.* **2012**, *22*, 21849–21851. [[CrossRef](#)]
22. Lu, G.; Li, S.; Guo, Z.; Farha, O.K.; Hauser, B.G.; Qi, X.; Wang, Y.; Wang, X.; Han, S.; Liu, X.; et al. Imparting functionality to a metal–organic framework material by controlled nanoparticle encapsulation. *Nat. Chem.* **2012**, *4*, 310–316. [[CrossRef](#)] [[PubMed](#)]
23. Chen, Y.; Zhai, B.; Liang, Y.; Li, Y. Hybrid photocatalysts using semiconductor/MOF/graphene oxide for superior photodegradation of organic pollutants under visible light. *Mater. Sci. Semicond. Process.* **2020**, *107*, 104838. [[CrossRef](#)]
24. Wang, X.; Zhao, S.; Zhang, Y.; Wang, Z.; Feng, J.; Song, S.; Zhang, H. CeO<sub>2</sub> nanowires self-inserted into porous Co<sub>3</sub>O<sub>4</sub> frameworks as high-performance “noble metal free” hetero-catalysts. *Chem. Sci.* **2016**, *7*, 1109–1114. [[CrossRef](#)] [[PubMed](#)]
25. Chen, L.; Chen, H.; Luque, R.; Li, Y. Metal–organic framework encapsulated Pd nanoparticles: Towards advanced heterogeneous catalysts. *Chem. Sci.* **2014**, *5*, 3708–3714. [[CrossRef](#)]
26. Peng, W.; Zheng, G.; Wang, Y.; Cao, S.; Ji, Z.; Huan, Y.; Zou, M.; Yan, X. Zn doped ZIF67-derived porous carbon framework as efficient bifunctional electrocatalyst for water splitting. *Int. J. Hydrog. Energy* **2019**, *44*, 19782–19791. [[CrossRef](#)]
27. Tuan, D.D.; Lin, K.Y.A. Ruthenium supported on ZIF-67 as an enhanced catalyst for hydrogen generation from hydrolysis of sodium borohydride. *Chem. Eng. J.* **2018**, *351*, 48–55. [[CrossRef](#)]
28. Wen, Y.; Wang, X.; Wei, H.; Li, B.; Jin, B.; Li, L. A large-scale continuous-flow process for the production of adipic acid via catalytic oxidation of cyclohexene with H<sub>2</sub>O<sub>2</sub>. *Green Chem.* **2012**, *14*, 2868–2875. [[CrossRef](#)]
29. Van de Vyver, S.; Román-Leshkov, Y. Emerging catalytic processes for the production of adipic acid. *Catal. Sci. Technol.* **2013**, *3*, 1465–1479. [[CrossRef](#)]
30. Adili, L.; Roufegarnejad, L.; Tabibiazar, M.; Hamishehkar, H.; Alizadeh, A. Development and characterization of reinforced ethyl cellulose based oleogel with adipic acid: Its application in cake and beef burger. *LWT Food Sci. Technol.* **2020**, *126*, 109277. [[CrossRef](#)]
31. Vibha, K.; Negi, S. Enzymatic plasticising of lignin and styrene with adipic acid to synthesize a biopolymer with high antioxidant and thermostability. *Polym. Degrad. Stab.* **2020**, *174*, 109081. [[CrossRef](#)]
32. Acid, A. *World Market Outlook and Forecast up to 2027*; Merchant Research and Consulting Ltd.: Birmingham, UK, 2018.
33. Montzka, S.A.; Dlugokencky, E.J.; Butler, J.H. Non-CO<sub>2</sub> greenhouse gases and climate change. *Nature* **2011**, *476*, 43. [[CrossRef](#)] [[PubMed](#)]
34. ALINI, S.; BABINI, P. The Industrial Oxidation of KA Oil to Adipic Acid. In *Handbook of Advanced Methods and Processes in Oxidation Catalysis: From Laboratory to Industry*; World Scientific: Paris, France, 2014; pp. 320–333.
35. Mazzi, A.; Paul, S.; Cavani, F.; Wojcieszak, R. Cyclohexane Oxidation to Adipic Acid Under Green Conditions: A Scalable and Sustainable Process. *Chemcatchem* **2018**, *10*, 3680–3682. [[CrossRef](#)]
36. Shang, M. The Direct Synthesis of Adipic Acid from Cyclohexene and Hydrogen Peroxide by a Continuous Micro-Flow Process. Ph.D. Thesis, Technische Universiteit Eindhoven, Eindhoven, The Netherlands, 2016.
37. Lesage, G.; Penate, I.Q.; Cagnet, P.; Poux, M. Green process for adipic acid synthesis: Oxidation by hydrogen peroxide in water micromelusions using Benzalkonium Chloride C12-14 surfactant. *Int. J. Chem. React. Eng.* **2012**, *10*, 1–18. [[CrossRef](#)]
38. Deng, Y.; Ma, Z.; Wang, K.; Chen, J. Clean synthesis of adipic acid by direct oxidation of cyclohexene with H<sub>2</sub>O<sub>2</sub> over peroxytungstate–organic complex catalysts. *Green Chem.* **1999**, *1*, 275–276. [[CrossRef](#)]
39. Alcañiz-Monge, J.; Trautwein, G.; Garcia-Garcia, A. Influence of peroxometallic intermediaries present on polyoxometalates nanoparticles surface on the adipic acid synthesis. *J. Mol. Catal. A Chem.* **2014**, *394*, 211–216. [[CrossRef](#)]
40. Raj, K.; Partow, S.; Correia, K.; Khusnutdinova, A.N.; Yahunin, A.F.; Mahadevan, R. Biocatalytic production of adipic acid from glucose using engineered *Saccharomyces cerevisiae*. *Metab. Eng. Commun.* **2018**, *6*, 28–32. [[CrossRef](#)]
41. Liu, H.; Jiang, T.; Han, B.; Liang, S.; Zhou, Y. Selective phenol hydrogenation to cyclohexanone over a dual supported Pd–Lewis acid catalyst. *Science* **2009**, *326*, 1250–1252. [[CrossRef](#)]
42. Thomas, J.M.; Raja, R.; Jhonson, B.F.G.; O’Connell, T.J.; Sanakar, G.; Khimyak, T. Bimetallic nanocatalysts for the conversion of muconic acid to adipic acid. *Chem. Commun.* **2003**, 1126–1127. [[CrossRef](#)]
43. Zhao, R.; Ji, D.; Lv, G.; Qian, G.; Yan, L.; Wang, X.; Sou, J. A highly efficient oxidation of cyclohexane over Au/ZSM-5 molecular sieve catalyst with oxygen as oxidant. *Chem. Commun.* **2004**, *35*, 904–905. [[CrossRef](#)]
44. Cheng, C.Y.; Lin, K.J.; Prasad, M.R.; Fu, S.J.; Chang, S.Y.; Shyu, S.G.; Sheu, S.H.; Chen, C.H.; Chuang, C.H.; Lin, M.T. Synthesis of a reusable oxotungsten-containing SBA-15 mesoporous catalyst for the organic solvent-free conversion of cyclohexene to adipic acid. *Catal. Commun.* **2007**, *8*, 1060–1064. [[CrossRef](#)]
45. Saedi, Z.; Tangestaninejad, S.; Moghadam, M.; Mirkhani, V.; Muhammadpoor-Baltork, I. MIL-101 metal–organic framework: A highly efficient heterogeneous catalyst for oxidative cleavage of alkenes with H<sub>2</sub>O<sub>2</sub>. *Catal. Commun.* **2012**, *17*, 18–22. [[CrossRef](#)]
46. Timofeeva, M.N.; Kholdeeva, O.A.; Jhung, S.H.; Chang, J.S. Titanium and cerium-containing mesoporous silicate materials as catalysts for oxidative cleavage of cyclohexene with H<sub>2</sub>O<sub>2</sub>: A comparative study of catalytic activity and stability. *Appl. Catal. A* **2008**, *345*, 195–200. [[CrossRef](#)]
47. Kehoe, A.B.; Scanlon, D.O.; Watson, W. Role of lattice distortions in the oxygen storage capacity of divalently doped CeO<sub>2</sub>. *Chem. Mater.* **2011**, *23*, 4464–4468. [[CrossRef](#)]
48. Yang, D.; Wang, L.; Sun, Y.; Zhou, K. Synthesis of one-dimensional Ce<sub>1-x</sub>Y<sub>x</sub>O<sub>2-x/2</sub> (0 ≤ x ≤ 1) solid solutions and their catalytic properties: The role of oxygen vacancies. *J. Phys. Chem. C* **2010**, *114*, 8926–8932. [[CrossRef](#)]

49. Li, T.; Xiang, G.; Zhuang, J.; Wang, X. Enhanced catalytic performance of assembled ceria necklace nanowires by Ni doping. *Chem. Commun.* **2011**, *47*, 6060–6062. [[CrossRef](#)]
50. Qin, J.; Lu, J.; Cao, M.; Hu, C. Synthesis of porous CuO–CeO<sub>2</sub> nanospheres with an enhanced low-temperature CO oxidation activity. *Nanoscale* **2010**, *2*, 2739–2743. [[CrossRef](#)]
51. Lin, M.; Fu, Z.Y.; Tan, H.R.; Tan, J.P.Y.; Ng, S.C.; Teo, E. Hydrothermal synthesis of CeO<sub>2</sub> nanocrystals: Ostwald ripening or oriented attachment? *Cryst. Growth Des.* **2012**, *12*, 3296–3303. [[CrossRef](#)]
52. Jiang, Z.; Li, Z.; Qin, Z.; Sun, H.; Jiao, X.; Chen, D. LDH nanocages synthesized with MOF templates and their high performance as supercapacitors. *Nanoscale* **2013**, *5*, 11770–11775. [[CrossRef](#)]
53. Yang, F.; Wei, J.; Liu, W.; Guo, J.; Yang, Y. Copper doped ceria nanospheres: Surface defects promoted catalytic activity and a versatile approach. *J. Mater. Chem. A* **2014**, *2*, 5662–5667. [[CrossRef](#)]
54. Wu, H.; Qian, X.; Zhu, H.; Ma, S.; Zhu, G.; Long, Y. Controlled synthesis of highly stable zeolitic imidazolate framework-67 dodecahedra and their use towards the templated formation of a hollow Co<sub>3</sub>O<sub>4</sub> catalyst for CO oxidation. *RSC Adv.* **2016**, *6*, 6915–6920. [[CrossRef](#)]
55. Wu, Z.; Sun, L.P.; Yang, M.; Huo, L.H.; Zhao, H.; Grenier, J.C. Facile synthesis and excellent electrochemical performance of reduced graphene oxide–Co<sub>3</sub>O<sub>4</sub> yolk-shell nanocages as a catalyst for oxygen evolution reaction. *J. Mater. Chem. A* **2016**, *4*, 13534–13542. [[CrossRef](#)]
56. Chen, W.; Li, F.; Yu, J. Combustion synthesis and characterization of nanocrystalline CeO<sub>2</sub>-based powders via ethylene glycol–nitrate process. *Mater. Lett.* **2006**, *60*, 57–62. [[CrossRef](#)]
57. Kumar, K.S.; Jaya, N.V. Synthesis and Characterization of Pure and Sn-Doped CeO<sub>2</sub> Nanoparticles. *Asian J. Chem.* **2013**, *25*, 6095–6098. [[CrossRef](#)]
58. Yang, X.; Chen, J.; Chen, Y.; Feng, P.; Lai, H.; Li, J.; Luo, X. Novel Co<sub>3</sub>O<sub>4</sub> nanoparticles/nitrogen-doped carbon composites with extraordinary catalytic activity for oxygen evolution reaction (OER). *Nanomicro Lett.* **2018**, *10*, 15. [[CrossRef](#)]
59. Xu, Q.; Lei, W.; Li, X.; Qi, X.; Yu, J.; Liu, G.; Wang, J.; Zhang, P. Efficient removal of formaldehyde by nanosized gold on well-defined CeO<sub>2</sub> nanorods at room temperature. *Environ. Sci. Technol.* **2014**, *48*, 9702–9708. [[CrossRef](#)]
60. Briggs, D. *Practical Surface Analysis Auger and X-ray Photoelectron Spectroscopy*, 2nd ed.; John Wiley: New York, NY, USA, 1990; Volume 1, p. 657.
61. Kim, M.H.; Choo, K.H. Low-temperature continuous wet oxidation of trichloroethylene over CoOx/TiO<sub>2</sub> catalysts. *Catal. Commun.* **2007**, *8*, 462–466. [[CrossRef](#)]
62. Liu, X.; Yang, H.; Han, L.; Liu, W.; Zhang, C.; Zhang, X.; Wang, S.; Yang, Y. Mesoporous-shelled CeO<sub>2</sub> hollow nanospheres synthesized by a one-pot hydrothermal route and their catalytic performance. *Cryst. Eng. Comm.* **2013**, *15*, 7769–7775. [[CrossRef](#)]
63. Xue, L.; Zhang, C.; He, H.; Teraoka, Y. Catalytic decomposition of N<sub>2</sub>O over CeO<sub>2</sub> promoted Co<sub>3</sub>O<sub>4</sub> spinel catalyst. *Appl. Catal. B* **2007**, *75*, 167–174. [[CrossRef](#)]
64. Martínez, L.; Roman, E.; De Segovia, J.L.; Poupard, S.; Creus, J.; Pedraza, F. Surface study of cerium oxide based coatings obtained by cathodic electrodeposition on zinc. *Appl. Surf. Sci.* **2011**, *257*, 6202–6207. [[CrossRef](#)]
65. Qian, J.; Chen, F.; Zhao, X.; Chen, Z. China rose petal as biotemplate to produce two-dimensional ceria nanosheets. *J. Nanopart. Res.* **2011**, *13*, 7149–7158. [[CrossRef](#)]
66. Park, K.S.; Jin, S.; Kang, K.H.; Lee, J.; Song, I.; Lee, B.S.; Kim, S.; Sohn, J.; Pak, C.; Kim, G.; et al. Characterization of Zeolitic Imidazolate Framework-Derived Polyhedral Carbonaceous Material and Its Application to Electrocatalyst for Oxygen Reduction Reaction. *Int. J. Electrochem. Sci.* **2016**, *11*, 9295–9306. [[CrossRef](#)]
67. Ma, G.; Li, C.; Liu, F.; Majeed, M.K.; Feng, Z.; Cui, Y.; Yang, J.; Qian, Y. Metal-organic framework-derived Co<sub>0.85</sub>Se nanoparticles in N-doped carbon as a high-rate and long-lifespan anode material for potassium ion batteries. *Mater. Today Energy* **2018**, *10*, 241–248.
68. Kuruppathparambil, R.R.; Jose, T.; Babu, R.; Hwang, G.Y.; Kathalikkatail, A.C.; Kim, D.W.; Park, D.W. A room temperature synthesizable and environmental friendly heterogeneous ZIF-67 catalyst for the solvent less and co-catalyst free synthesis of cyclic carbonates. *Appl. Catal. B* **2016**, *182*, 562–569. [[CrossRef](#)]
69. Lee, H.; Ko, J.H.; Kwon, W.H.; Park, Y.K. Conversion of acetic acid from the catalytic pyrolysis of xylan over CeO<sub>2</sub>. *J. Nanosci. Nanotechnol.* **2016**, *16*, 4480–4482. [[CrossRef](#)] [[PubMed](#)]
70. Liu, S.; Wu, X.; Liu, W.; Chen, W.; Ran, R.; Li, M.; Weng, D. Soot oxidation over CeO<sub>2</sub> and Ag/CeO<sub>2</sub>: Factors determining the catalyst activity and stability during reaction. *J. Catal.* **2016**, *337*, 188–198. [[CrossRef](#)]
71. Sato, K.; Aoki, M.; Noyori, R. A “green” route to adipic acid: Direct oxidation of cyclohexenes with 30 percent hydrogen peroxide. *Science* **1998**, *281*, 1646–1647. [[CrossRef](#)]
72. Wang, L.; Wan, C.; Fu, Y.; Chen, H.; Liu, X.; Li, M. Study on the effects of adipic acid on properties of dicyandiamide-cured electrically conductive adhesive and the interaction mechanism. *J. Electron. Mater.* **2014**, *43*, 132–136. [[CrossRef](#)]
73. Vafaezadeh, M.; Hashemi, M.M. One pot oxidative cleavage of cyclohexene to adipic acid using silver tungstate nano-rods in a Brønsted acidic ionic liquid. *RSC Adv.* **2015**, *5*, 31298–31302. [[CrossRef](#)]
74. Vafaezadeh, M.; Hashemi, M.M. Simple and green oxidation of cyclohexene to adipic acid with an efficient and durable silica-functionalized ammonium tungstate catalyst. *Catal. Commun.* **2014**, *43*, 169–172. [[CrossRef](#)]
75. Agúndez, J.; Ares, C.; Márquez-Álvarez, C.; Pariente, J.P. Catalytic oxidation of cyclohexene by supported gold nanoclusters synthesized in a two-liquid phases system containing eucalyptus essential oil. *Mol. Catal.* **2020**, *488*, 110922. [[CrossRef](#)]

76. Chizallet, C.; Lazare, S.; Bazer-Bachi, D.; Bonnier, F.; Lecocq, V.; Soyer, E.; Quoinead, A.A.; Bats, N. Catalysis of transesterification by a nonfunctionalized metal–organic framework: Acido-basicity at the external surface of ZIF-8 probed by FTIR and ab initio calculations. *J. Am. Chem. Soc.* **2010**, *132*, 12365–12377. [[CrossRef](#)] [[PubMed](#)]
77. Mousavi, B.; Chaemcheun, S.; Moosavi, B.; Luo, Z.; Gholampur, N.; Verpoort, F. Zeolitic imidazole framework-67 as an efficient heterogeneous catalyst for the conversion of CO<sub>2</sub> to cyclic carbonates. *New J. Chem.* **2016**, *40*, 5170–5176. [[CrossRef](#)]
78. Dai, J.; Guo, Y.; Xu, L.; Zhuang, G.; Zheng, Y.; Sun, D.; Huang, J.; Li, Q. Bovine serum albumin templated porous CeO<sub>2</sub> to support Au catalyst for benzene oxidation. *Mol. Catal.* **2020**, *486*, 110849. [[CrossRef](#)]
79. Wang, X.; Liu, D.; Li, J.; Zhen, J.; Zhang, H. Clean synthesis of Cu<sub>2</sub>O@ CeO<sub>2</sub> core@ shell nanocubes with highly active interface. *NPG Asia Mater.* **2015**, *7*, e158. [[CrossRef](#)]
80. Cai, W.; Chen, F.; Shen, X.; Chen, L.; Zhang, J. Enhanced catalytic degradation of AO7 in the CeO<sub>2</sub>–H<sub>2</sub>O<sub>2</sub> system with Fe<sup>3+</sup> doping. *Appl. Catal. B* **2010**, *101*, 160–168. [[CrossRef](#)]
81. Ji, P.; Wang, L.; Chen, F.; Zhang, J. Ce<sup>3+</sup>-centric organic pollutant elimination by CeO<sub>2</sub> in the presence of H<sub>2</sub>O<sub>2</sub>. *ChemCatChem* **2010**, *2*, 1552–1554. [[CrossRef](#)]
82. Kuruppathparambil, R.R.; Babu, R.; Jeong, H.M.; Hwang, G.Y.; Jeong, G.S.; Kim, M.; Kim, D.W.; Park, D.W. A solid solution zeolitic imidazolate framework as a room temperature efficient catalyst for the chemical fixation of CO<sub>2</sub>. *Green Chem.* **2016**, *18*, 6349–6356. [[CrossRef](#)]
83. Jose, T.; Hwang, Y.; Kim, D.W.; Kim, M.; Park, D.W. Functionalized zeolitic imidazolate framework F-ZIF-90 as efficient catalyst for the cycloaddition of carbon dioxide to allyl glycidyl ether. *Catal. Today* **2015**, *245*, 61–67. [[CrossRef](#)]
84. Fang, W.; Chen, J.; Zhou, X.; Chen, J.; Ye, Z.; Li, Y. Zeolitic Imidazolate Framework-67 Derived CeO<sub>2</sub>@ Co<sub>3</sub>O<sub>4</sub> Core-shell Microspheres with Enhanced Catalytic Activity towards Toluene Oxidation. *Ind. Eng. Chem. Res.* **2020**, *59*, 10328–10337. [[CrossRef](#)]
85. Kan, J.; Deng, L.; Li, B.; Huang, Q.; Zhu, S.; Shen, S.; Chen, Y. Performance of co-doped Mn-Ce catalysts supported on cordierite for low concentration chlorobenzene oxidation. *Appl. Catal. A* **2017**, *530*, 21–29. [[CrossRef](#)]
86. Rao, B.G.; Sudarsanam, P.; Nallappareddy, P.R.G.; Reddy, M.Y.; Rao, T.V.; Reddy, B.M. Selective allylic oxidation of cyclohexene over a novel nanostructured CeO<sub>2</sub>–Sm<sub>2</sub>O<sub>3</sub>/SiO<sub>2</sub> catalyst. *Res. Chem. Intermed.* **2018**, *44*, 6151–6168. [[CrossRef](#)]
87. Hakat, Y.; Kotbagi, T.V.; Bakker, M.G. Silver supported on hierarchically porous SiO<sub>2</sub> and Co<sub>3</sub>O<sub>4</sub> monoliths: Efficient heterogeneous catalyst for oxidation of cyclohexene. *J. Mol. Catal. A Chem.* **2016**, *411*, 61–71. [[CrossRef](#)]
88. Acharyya, S.S.; Ghosh, S.; Bal, R. Nanoclusters of Cu (II) supported on nanocrystalline W (VI) oxide: A potential catalyst for single-step conversion of cyclohexane to adipic acid. *Green Chem.* **2015**, *17*, 3490–3499. [[CrossRef](#)]
89. Soares, J.C.S.; Gonçalves, A.H.A.; Zotin FM, Z.; Araújo, L.R.R.; Gaspar, A.B. Cyclohexene to adipic acid synthesis using heterogeneous polyoxometalate catalysts. *Mol. Catal.* **2018**, *458*, 223–229. [[CrossRef](#)]
90. Lesage, G.; Peñate, I.Q.; Franceschi, S.; Perez, E.; Garrigues, J.C.; Poux, M.; Cognet, P. Sustainable process for adipic acid production from cyclohexene in microemulsion. *Catal. Today* **2019**, *346*, 40–45. [[CrossRef](#)]
91. Moreno, I.; Navascues, N.; Irusta, S.; Santamaria, J. Electrospun Au/CeO<sub>2</sub> nanofibers: A highly accessible low-pressure drop catalyst for preferential CO oxidation. *J. Catal.* **2015**, *329*, 479–489. [[CrossRef](#)]